Nuclear Science and Techniques (2025) 36:38
https://doi.org/10.1007/s41365-024-01597-w

Improvement and correction for transverse emittance diagnosis based on *Q*-scanning techniques

Yi-Feng Zeng[1] · Hao Hu[1] · Tong-Ning Hu[1]

Received: 14 November 2023 / Revised: 22 March 2024 / Accepted: 27 April 2024 / Published online: 27 January 2025

Abstract
Precise transverse emittance assessment in electron beams is crucial for advancing high-brightness beam injectors. As opposed to intricate methodologies that use specialized devices, quadrupole focusing strength scanning (*Q*-scanning) techniques offer notable advantages for various injectors owing to their inherent convenience and cost-effectiveness. However, their stringent approximation conditions lead to inevitable errors in practical operation, thereby limiting their widespread application. This study addressed these challenges by revisiting the analytical derivation procedure and investigating the effects of the underlying approximation conditions. Preliminary corrections were explored through a combination of data processing analysis and numerical simulations. Furthermore, based on theoretical derivations, virtual measurements using beam dynamics calculations were employed to evaluate the correction reliability. Subsequent experimental validations were performed at the Huazhong University of Science and Technology injector to verify the effectiveness of the proposed compensation method. Both the virtual and experimental results confirm the feasibility and reliability of the enhanced *Q*-scanning-based diagnosis for transverse emittance in typical beam injectors operating under common conditions. Through the integration of these corrections and compensations, enhanced *Q*-scanning-based techniques emerge as promising alternatives to traditional emittance diagnosis methods.

Keywords Beam diagnostics · Transverse emittance · *Q*-scanning technique · Beam injector

1 Introduction

High-quality electron beams are crucial for advancing current research and industrial applications [1–5]. The performance of facilities in this domain is highly dependent on accelerator-based injectors, which generate the electron beams. Specifically, research facilities, such as free-electron lasers (FELs), synchrotron radiation lasers (SRLs), and ultrafast electron diffraction (UED) systems, rely heavily on injectors as key components because they directly affect the overall performance and application capabilities of such setups [4–8].

To comprehensively understand the underlying physics of high-brightness electron beams and further promote the development and application of the associated beam injectors, accurate measurements of primary beam parameters, such as the energy, energy spread, bunch length, and transverse emittance, are essential for injector commissioning and performance optimization [9–15]. Among beam parameters, the transverse emittance, a metric derived from the beam distribution in the phase space that quantifies its divergence and focusing ability, serves as a crucial indicator for evaluating injector performance, particularly for scientific research applications [15, 16]. Consequently, significant research efforts have been directed toward transverse emittance and phase-space characterization, with the ultimate goal of enhancing emittance diagnosis and minimization techniques, which will ultimately benefit numerous beam injectors [15–18].

This work was supported by the National Natural Science Foundation of China (Nos. 12341501 and 11905074).

✉ Tong-Ning Hu
TongningHu@hust.edu.cn

[1] State Key Laboratory of Advanced Electromagnetic Technology, School of Electrical and Electronic Engineering, Huazhong University of Science and Technology, Wuhan 430074, China

Several methods exist for transverse emittance characterization, with emerging techniques using deflection cavities capable of slice emittance measurements [19–21]. However, these methods often involve complex peripheral systems. In contrast, traditional emittance measurement methods, including the pepper-pot, multi-slit, multi-screen, and quadrupole magnet scanning (Q-scanning) methods, have a well-established foundation and offer simpler setups. Among these methods, the former two are primarily suitable for beam emittance measurements in the presence of space-charge effects [22–25]. However, they require high-precision machining of the insertion devices. In contrast, the multi-screen method is based on observing the beam size at different locations along a beamline for emittance measurement [26], which may prolong the beamline length. The Q-scanning method relies on analyzing changes in the beam size in response to variations in the focusing strength of Q-magnets [27]. More importantly, the Q-scanning method can utilize existing Q-magnets commonly installed on the downstream beamline of the injector, thereby simplifying the diagnosis system and improving its robustness.

Nevertheless, for facilities such as FELs and UED systems that require low transverse emittance, the Q-scanning method suffer shortcomings in terms of measurement accuracy. This limitation stems from its reliance on multiple approximations. Consequently, previous studies have explored the impact of various parameters on measurement accuracy and delved into the statistical and systematic error evaluation, as well as the handling of space-charge and chromatic effects [28–33].

Accordingly, based on a comprehensive examination of the fundamental principles and approximation conditions inherent in the Q-scanning method, we investigated the impacts of these assumptions and explored practical correction and compensation approaches for measurement accuracy improvement. Theoretical derivations were systematically performed and rigorously verified through beam dynamics simulations in terms of virtual measurements using the beam parameters of an injector established at Huazhong University of Science and Technology (HUST) as a test case. The proposed method was also implemented on a HUST injector for experimental validation. The findings of this study demonstrate that the proposed integrated methodology significantly improves the precision of Q-scanning.

2 Brief review of the Q-scanning technique

2.1 Basic theory

As highlighted in the preceding section, owing to its inherent advantages, including cost-effectiveness, system stability, and simplicity, the Q-scanning method has been extensively used in emittance measurements across various beam injectors.

As shown in Fig. 1, a Q-magnet is used to focus the beam in either the horizontal or vertical direction onto a downstream Fluorscreen [34]. The beam distribution on the Fluorscreen is measured by capturing the optical transition light generated when the beam passes through the Fluorscreen. Through iterative adjustments of the focusing strength parameter K of the Q-magnet and simultaneous measurement of the corresponding beam cross-sectional sizes intercepted by the Fluorscreen, it is possible to use the beam transport principles to calculate the transverse emittance. In practical measurements employing a particle statistical model, the subsequent analysis describes the beam parameters using root-mean-square (rms) values, denoted as $\sigma(...)$, while the average values are represented as $\langle ... \rangle$. The beam spot size on the Fluorscreen $\sigma(x_1)$ can be expressed in terms of the initial beam parameters and transfer matrix elements R_{11} and R_{12} as follows:

$$\begin{aligned}\sigma^2(x_1) &= \langle x_1^2 \rangle \\ &= R_{11}^2\sigma^2(x_0) + R_{12}^2\sigma^2(x_0') + 2R_{11}R_{12}\langle x_0 x_0' \rangle \\ &= \varepsilon_0\left[R_{11}^2\beta_0 - 2R_{11}R_{12}\alpha_0 + R_{12}^2\gamma_0\right],\end{aligned} \tag{1}$$

where x and x' denote variations in the transverse position and divergence relative to the central particle, respectively. In the statistical model, $\sigma(x_0)$ denotes the initial transverse size of the beam at the entrance of the measuring system and $\sigma(x_0')$ and $\sqrt{\langle x_0 x_0' \rangle}$ denote the initial transverse divergence and correlation, respectively. Simultaneously, the initial Twiss parameters are α_0, β_0 and γ_0, where ε_0 denotes the transverse emittance to be determined.

$$\begin{cases} R_{11} = \cos\left(\sqrt{k}L_Q\right) - L_d\sqrt{k}\sin\left(\sqrt{k}L_Q\right) \\ R_{12} = \sin\left(\sqrt{k}L_Q\right)\Big/\sqrt{k} + L_d\cos\left(\sqrt{k}L_Q\right) \end{cases} \tag{2}$$

where L_Q and L_d denote the effective length of the Q-magnet and downstream drifting distance, respectively. The

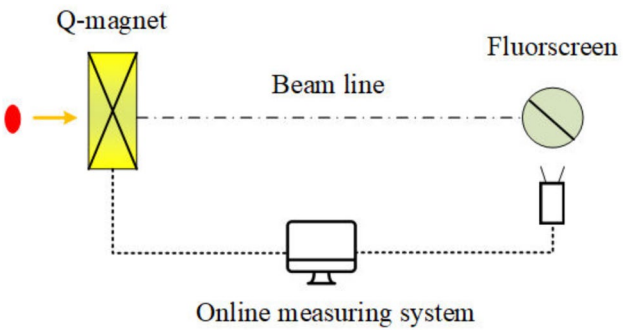

Fig. 1 Emittance measurement system

Q-magnet's focusing parameter is defined as $k = \frac{1}{B\rho}\frac{\partial B}{\partial r}(1/\mathrm{m}^2) = \frac{299.792g(\mathrm{T/m})}{E(\mathrm{MeV})}$, where $B\rho$ denotes the magnetic rigidity, E denotes the beam energy, and g represents the magnetic field gradient determined by the inherent properties of the Q-magnet and its current value.

In accordance with Eqs. (1) and (2), by measuring the beam spot sizes corresponding to three different sets of K values, the equation set can be solved to determine the Twiss parameters, subsequently allowing the emittance calculation.

2.2 Thin-lens approximation

Although the equation set given in the previous subsection provides a means to measure the beam emittance, it is noteworthy that this method is susceptible to relatively large errors. In particular, when $K = kL_Q$ is close to zero, the emittance measurement system can employ the thin-lens approximation, where the transfer matrix elements, specifically R_{11} and R_{12}, are approximated as

$$\begin{cases} R_{11} = 1 - KL_\mathrm{d} \\ R_{12} = L_\mathrm{d} \end{cases} \tag{3}$$

Based on the aforementioned statements, Eq. (1) can be reformulated as Eq. (4) by substituting Eq. (3). Subsequently, this can be simplified to obtain Eq. (5) as follows:

$$\sigma^2(x_1) = \varepsilon_0\left[\left(1 - KL_\mathrm{d}\right)^2\beta_0 - 2\left(1 - KL_\mathrm{d}\right)L_\mathrm{d}\alpha_0 + L_\mathrm{d}^2\gamma_0\right], \tag{4}$$

$$\sigma^2(x_1) = a(K-b)^2 + c = aK^2 - 2abK + ab^2 + c\,. \tag{5}$$

A parabolic relationship exists between $\sigma^2(x_1)$ and K, and the corresponding coefficients are as follows:

$$a = \varepsilon_0 L_\mathrm{d}^2\beta_0 \quad b = \frac{(\beta_0 L_\mathrm{d} - L_\mathrm{d}^2\alpha_0)}{\beta_0 L_\mathrm{d}^2}, \quad c = \frac{\varepsilon_0 L_\mathrm{d}^2}{\beta_0}\,. \tag{6}$$

Hence, the transverse emittance along with the Twiss parameters at the entrance of the Q-scanning system can be succinctly characterized by the following parabolic coefficients:

$$\varepsilon_0 = \frac{\sqrt{ac}}{L_\mathrm{d}^2}, \quad \alpha_0 = \sqrt{\frac{a}{c}}\left(-b + \frac{1}{L_\mathrm{d}}\right), \quad \beta_0 = \sqrt{\frac{a}{c}}\,. \tag{7}$$

Therefore, as a common practice to mitigate measurement errors and improve the precision, rather than solving the equation set, it is customary to employ a parabolic fitting approach. This involves acquiring 10–15 sets of beam size data [27] and employing parabolic fitting techniques to determine the emittance.

3 Preliminary corrections

3.1 Corrections via fixed parabola vertex

As discussed in the previous subsection, when employing the thin-lens approximation, determining the emittance through parabolic fitting is feasible. However, various fitting errors may arise across the diverse ranges of independent variables, leading to inconsistent measurement outcomes. The conventional strategy involves collecting multiple data points in proximity to the focal point for fitting, requiring the initial identification of the focal point.

For convenience, let us define the focus size as $\sigma_{\mathrm{f,min}}(x)$, with independent variable $K_0 = f_{\mathrm{min}}^{-1}$. Here, f_{min} denotes the focal length. Then, Eq. (4) can be expressed as

$$\sigma^2(x_1) = \sigma_{\mathrm{f,min}}^2(x) + \frac{L_\mathrm{d}^4}{\sigma_{\mathrm{f,min}}^2(x)}\varepsilon_0^2(K - K_0)^2\,. \tag{8}$$

Accordingly, the coefficients in the original parabolic fitting equation correspond to

$$a = \frac{L_\mathrm{d}^4}{\sigma_{\mathrm{f,min}}^2(x)}\varepsilon_0^2, \mathrm{b} = \frac{1}{f_{\mathrm{min}}}, \mathrm{c} = \sigma_{\mathrm{f,min}}^2(x)\,. \tag{9}$$

Subsequently, the emittance can be calculated using a much simpler formula, as follows:

$$\varepsilon_0 = \frac{\sqrt{ac}}{L_\mathrm{d}^2}\,. \tag{10}$$

To examine and contrast the influence of the independent variable range for K on the emittance measurement results, the beam parameters of the HUST injector [35], as listed in Table 1, serve as an illustrative example. The setting parameters of the Q-scanning system employed in the HUST injector are also listed in Table 1.

To streamline the analysis and concentrate on examining the errors arising from the thin-lens approximation, the beam parameters were directly substituted into the complete transfer matrix of the Q-scanning system of the HUST injector. By varying K, multiple sets of beam spot sizes were generated at the system exit. This approach allowed us to comprehensively understand the impact of the thin-lens approximation on the system's performance.

Three parabolas are shown In Fig. 2a, each fitted to a distinct range of K values. Notably, the fitted parabolic

Table 1 Main setting parameters for the HUST injector

Parameter	Simulation results	Measurement results
Beam energy	14.0 MeV	13.7 MeV
Energy spread	0.27%	0.41%
Nor. transverse emittance	4.9 mm mrad	8.8 mm mrad

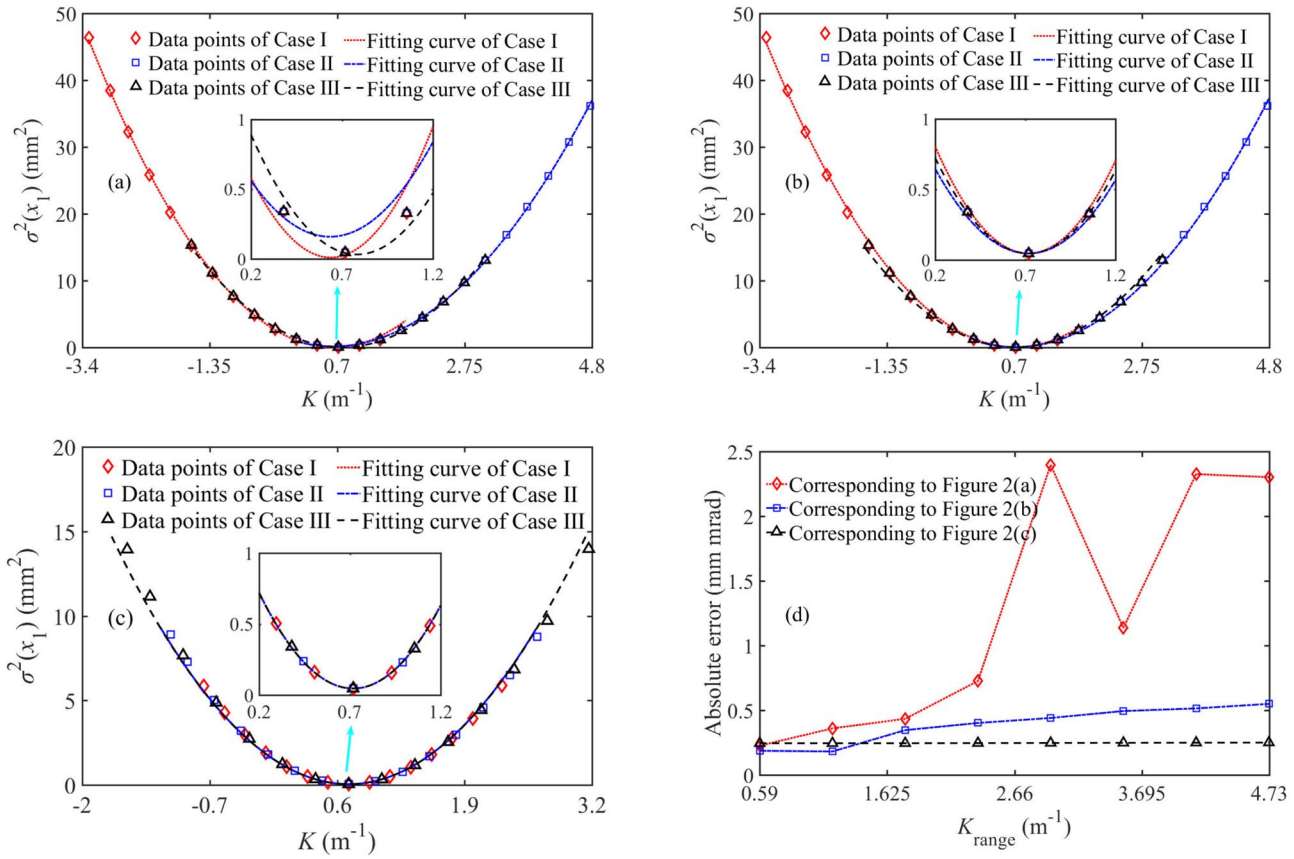

Fig. 2 Parabolic fitting results under different ranges of K values: **a** Arbitrary range (Case I: $K = -3.29 \sim 1.39\,\mathrm{m}^{-1}$, Case II: $K = -1.65 \sim 3.08\,\mathrm{m}^{-1}$, Case III: $K = 0.04 \sim 4.77\,\mathrm{m}^{-1}$); **b** Fixed vertex, range identical to that in **a**; **c** Fixed vertex with symmetric sampling (Case I: $K = -0.76 \sim 2.20\,\mathrm{m}^{-1}$, Case II: $K = -1.20 \sim 2.64\,\mathrm{m}^{-1}$, Case III: $K = -1.65 \sim 3.08\,\mathrm{m}^{-1}$); **d** Measurement error curves

vertices do not coincide when K assumes values in different ranges, suggesting that the K values corresponding to the focus points are different. For comparison, Fig. 2b shows the parabolic fitting curves under a fixed vertex, maintaining the approach of selecting points for K as in Fig. 2a. It can be seen that, although the overlap of the fitted parabolas in Fig. 2b is enhanced compared with that in Fig. 2a, the parabolas exhibit inconsistencies because they deviate from their vertices. Consequently, this inevitably introduces disparities in the emittance measurements determined by their coefficients.

To further elucidate this issue, the measurement errors induced by the two fitting methods are shown in Fig. 2d, where the abscissa $K_{\mathrm{range}} = K_{\mathrm{max}} - K_{\mathrm{min}}$ denotes the maximum K scanning range. The vertical axis in Fig. 2 indicates the absolute error of the measured emittance. By examining the measurement errors represented by the red dotted line in Fig. 2a, it is evident that despite setting K at equally spaced values in accordance with operational practices during actual measurements, varying K_{range} contributes to inconsistencies in the measurement errors, with an increasing trend as K_{range} increases.

For the method illustrated in Fig. 2b. The errors and their inconsistencies, as denoted by the dotted blue line in Fig. 2d, are notably reduced. In other words, fixing the parabolic vertex can significantly reduce both the measurement errors and their inconsistencies in the Q-scanning method. Nevertheless, it is noteworthy that the measurement error exhibits a gradual increase with K_{range}.

To address this issue more effectively, considering the distinctive characteristics of parabolic fitting errors and keeping the vertex fixed, we opted to select points symmetrically on both sides of the vertex. The data fitted using this method resulted in a series of parabolas, as shown in Fig. 2c. Notably, the parabolas obtained through this approach exhibited substantial overlap, and their measurement error consistency was significantly enhanced, as shown in Fig. 2d.

To analyze the impact of a small-size resolution, for beam spots near the vertex smaller than 0.1 mm, we set their sizes to 0.1 mm in the parabola fitting process (the optical system

resolution for beam spot measurements is generally better than 0.05 mm), as shown in Fig. 3a. The corresponding error analyses of the different data processing methods for small and indistinguishable vertex sizes are shown in Fig. 3b. When the beam spot size resolution was 0.1 mm, the proposed fixed vertex fitting method was suitable for beams with an initial normalized emittance greater than 2 mm mrad.

3.2 Chromatic effect correction

In the realm of beam injectors designed for diverse applications, the energy spread exhibits a considerable range, from a fraction of a percent to a few percent. When a beam characterized by significant energy spread traverses a *Q*-magnet, the quadrupole kick undergoes variations within the bunch itself, inducing transverse emittance changes [31]. Consequently, this chromatic effect introduces additional errors into the emittance measurements. Therefore, it is advantageous to correct the transfer matrix of the *Q*-scanning system, leading to rewriting Eq. (3) as follows:

$$\begin{cases} R_{11} = 1 - K(1-\delta)L_{\mathrm{d}} \\ R_{12} = L_{\mathrm{d}} \end{cases} \tag{11}$$

where $\delta = \Delta p/p$ represents the energy deviation relative to the central particle, and $\sigma(\delta)$ denotes the energy spread within the statistical model. Therefore, substituting Eqs. (11) into (1), the beam spot size at the downstream Fluorscreen yields

$$\sigma^2(x_1) = \sigma^2_{\delta=0}(x_1) + (KL_{\mathrm{d}})^2\sigma^2(\delta x_0) + 2KL_{\mathrm{d}}(1-KL_{\mathrm{d}})\langle \delta x_0^2\rangle + 2KL_{\mathrm{d}}^2\langle \delta x_0 x_0'\rangle, \tag{12}$$

where $\sigma^2_{\delta=0}(x_1)$ denotes the beam spot size and neglects the energy spread. We assumed that there is no correlation between the longitudinal and transverse properties, namely, $\langle \delta x_0^2\rangle = \langle \delta x_0 x_0'\rangle = 0$ and $\langle \delta^2 x_0^2\rangle = \langle \delta^2\rangle\langle x_0^2\rangle$. Then, Eq. (12) can be simplified by using the Twiss parameters as follows:

$$\sigma^2(x_1) = \sigma^2_{\delta=0}(x_1) + (KL_{\mathrm{d}})^2\varepsilon_0\beta_0\sigma^2(\delta)\,. \tag{13}$$

Therefore, the coefficients obtained from the fitting parabolic formula are

$$\begin{cases} a = \beta_0\varepsilon_0\big(1+\sigma^2(\delta)\big)L_{\mathrm{d}}^2, \\ b = \frac{-(L_{\mathrm{d}}\alpha_0-\beta_0)}{\beta_0\left(1+\sigma^2(\delta)\right)L_{\mathrm{d}}}, \\ c = \varepsilon_0\left[\beta_0 - 2L_{\mathrm{d}}\alpha_0 + L_{\mathrm{d}}^2\gamma_0 - \frac{(L_{\mathrm{d}}\alpha_0-\beta_0)^2}{\beta_0\left(1+\sigma^2(\delta)\right)}\right] \end{cases} \tag{14}$$

Subsequently, by combining $\gamma_0 = \frac{1+\alpha_0^2}{\beta_0}$, the emittance considering the influence of the energy spread can be solved.

Furthermore, to ascertain the efficiency of this correction method, beam dynamics simulations were performed using the HUST injector system parameters listed in Table 1. These simulations were executed in tandem with ASTRA [36]. It is worth noting that for practical relevance, in subsequent discussion, the magnetic field of the scanning *Q*-magnet at the HUST injector is incorporated into the beam dynamics software ASTRA. The corresponding simulation results are shown in Fig. 4.

Note that the correction method with fixed vertices and symmetric *K* values at equal intervals, as stated in Sect. 3.1, is conventionally adopted during the simulation process. As shown in Fig. 4a and b, the measurement errors remain consistent, regardless of the chromatic effect correction. Under this correction, a significant reduction in the influence of $\sigma(\delta)$ on the measurement errors is observed. Furthermore, a larger energy spread corresponds to a more pronounced correction effect. For example, when the energy spread is 6%, the relative measurement error decreases from approximately 12.5–7%, highlighting a significantly improved

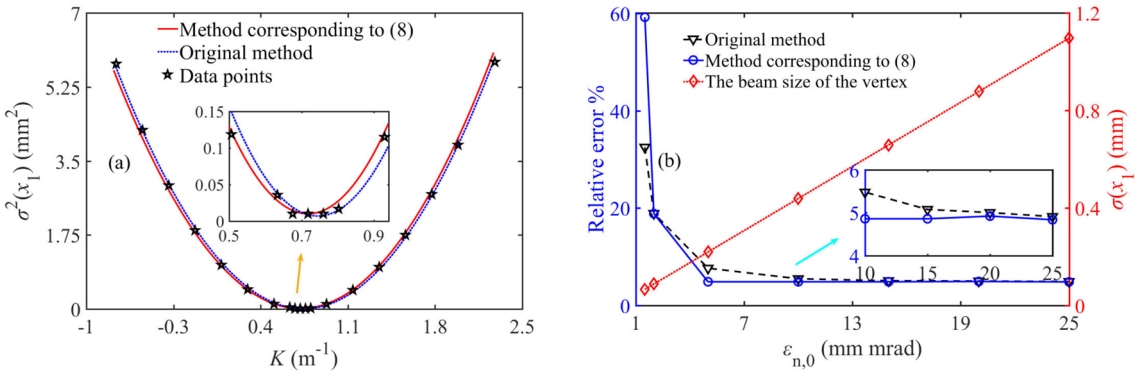

Fig. 3 **a** Parabola fitting curves and **b** error analysis for different data processing methods under small and indistinguishable vertex sizes

correction performance. In summary, the theoretical and simulation results collectively indicate a substantial reduction in emittance measurement errors and their inconsistencies by applying the proposed correction methods.

4 Improvement using second-order terms

4.1 Theoretical analysis

As discussed in Sect. 2, the traditional Q-scanning method relies on thin-lens approximation, where $\sqrt{k}L_Q \to 0$, and only the linear terms of the system transfer matrix elements are considered. However, for beam injectors operating at approximately 10 MeV, shorter beam transport lines are preferred to mitigate the space-charge effect impact. Consequently, it is imperative to rectify the errors that stem from the aforementioned approximation. Therefore, considering the second-order terms R_{11} and R_{12}, the following equations can be formulated:

$$\begin{cases} R_{11} = 1 - K\left(\frac{1}{2}L_Q + L_\mathrm{d}\right) \\ R_{12} = L_\mathrm{d} + L_Q - \frac{1}{2}KL_QL_\mathrm{d} \end{cases} \tag{15}$$

After inserting Eqs. (15) into (1), the beam spot size can be expressed as in Eq. (16), the parabolic equation coefficients adhere to the conditions outlined in Eq. (17). Subsequently, the emittance is determined by incorporating the Twiss parameter relation $\gamma_0 = \frac{1+\alpha_0^2}{\beta_0}$.

$$\begin{aligned} \sigma^2(x_1) = &\left[1 - K\left(\frac{1}{2}L_Q + L_\mathrm{d}\right)\right]^2 \varepsilon_0\beta_0 + \left(L_\mathrm{d} + L_Q - \frac{1}{2}KL_QL_\mathrm{d}\right)^2 \varepsilon_0\gamma_0 \\ &- 2\left[1 - K\left(\frac{1}{2}L_Q + L_\mathrm{d}\right)\right]\left(L_\mathrm{d} + L_Q - \frac{1}{2}KL_QL_\mathrm{d}\right)\varepsilon_0\alpha_0 \end{aligned} \tag{16}$$

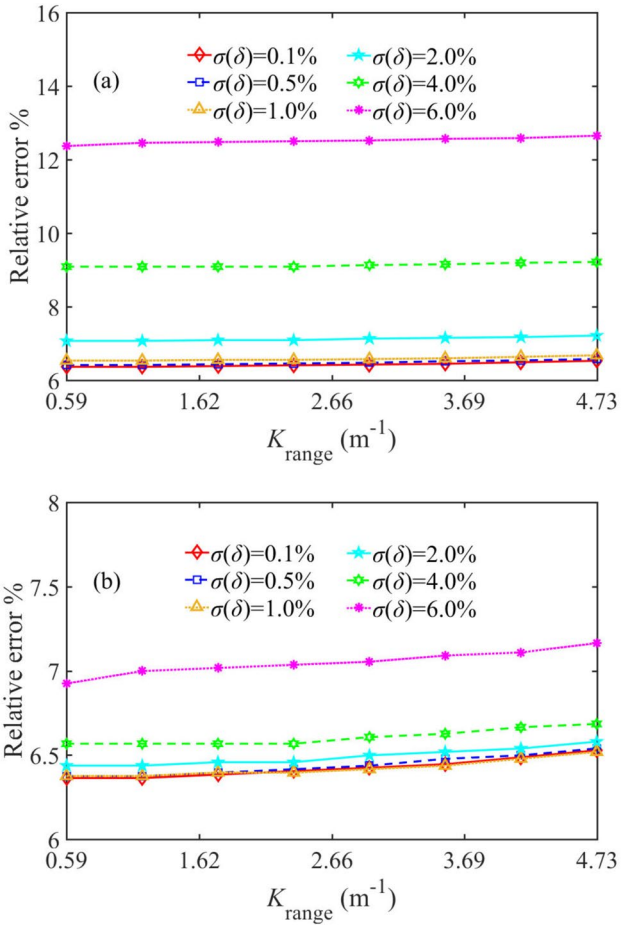

Fig. 4 Measurement error variations according to K_range for different $\sigma(\delta)$: **a** Traditional method corresponding to Eq. (8); **b** Correction method corresponding to Eq. (13)

$$\begin{cases} a = \varepsilon_0\left[\left(\frac{1}{2}L_Q + L_\mathrm{d}\right)^2\beta_0 - \left(\frac{1}{2}L_Q^2L_\mathrm{d} + L_QL_\mathrm{d}^2\right)\alpha_0 + \frac{1}{4}L_Q^2L_\mathrm{d}^2\gamma_0\right] \\ -2ab = \varepsilon_0\left[-\left(L_Q + 2L_\mathrm{d}\right)\beta_0 + 2\left(2L_QL_\mathrm{d} + \frac{1}{2}L_Q^2 + L_\mathrm{d}^2\right)\alpha_0 - \left(L_QL_\mathrm{d}^2 + L_Q^2L_\mathrm{d}\right)\gamma_0\right] \\ ab^2 + c = \varepsilon_0\left[\beta_0 - 2\left(L_\mathrm{d} + L_Q\right)\alpha_0 + \left(L_\mathrm{d}^2 + L_Q^2 + 2L_\mathrm{d}L_Q\right)\gamma_0\right] \end{cases} \tag{17}$$

Section 3.2 provides an in-depth examination of the effects of $\sigma(\delta)$; Eq. (15) can be rewritten as

$$\begin{cases} R_{11} = 1 - K\left(\frac{1}{2}L_Q + L_\mathrm{d}\right) + K\delta\left(\frac{1}{2}L_Q + L_\mathrm{d}\right) \\ R_{12} = L_\mathrm{d} + L_Q - \frac{1}{2}KL_QL_\mathrm{d} + \frac{1}{2}K\delta L_QL_\mathrm{d} \end{cases} \tag{18}$$

The beam spot size equation can be decomposed into two components: $\sigma^2(x_1) = \sigma^2_{\delta=0}(x_1) + \sigma^2_\delta(x_1)$, where $\sigma^2(x_1) = \sigma^2_{\delta=0}(x_1) + \sigma^2_\delta(x_1)$ denotes the spot size in the absence of a chromatic effect, which can be directly calculated using Eq. (16). Meanwhile, $\sigma^2_\delta(x_1)$ represents the contribution of $\sigma(\delta)$ to $\sigma^2(x_1)$. By substituting Eqs. (18) into (1) and integrating it with Eq. (16), a new expression for $\sigma^2(x_1)$ is obtained, as in Eq. (19). Subsequently, neglecting the longitudinal and transverse coupling enables the derivation of Eq. (20). Leveraging the parabolic fitting equation, the first coefficient in Eq. (17) is refined using Eq. (21), while the other two equations remain unchanged.

$$\begin{aligned}\sigma_\delta^2(x_1) = {} & K^2\left(\frac{1}{2}L_Q + L_\mathrm{d}\right)^2\sigma^2(\delta x_0) \\ & + \frac{1}{4}K^2L_Q^2L_\mathrm{d}^2\sigma^2(\delta x_0') + K^2L_Q^2L_\mathrm{d}^2\langle\delta^2 x_0x_0'\rangle \\ & + K(L_Q+2L_d)\left[1-K\left(\frac{1}{2}L_Q+L_\mathrm{d}\right)\right]\langle\delta x_0^2\rangle \\ & + KL_QL_\mathrm{d}\left(L_\mathrm{d}+L_Q-\frac{1}{2}KL_QL_\mathrm{d}\right)\langle\delta x_0'^2\rangle \\ & + K\left\{L_QL_\mathrm{d}\left[1-K\left(\frac{1}{2}L_Q+L_\mathrm{d}\right)\right]\right. \\ & \left.+(L_Q+2L_\mathrm{d})\left(L_\mathrm{d}+L_Q-\frac{1}{2}KL_QL_\mathrm{d}\right)\right\}\langle\delta x_0x_0'\rangle\end{aligned} \tag{19}$$

$$\begin{aligned}\sigma^2(x_1) = {} & \sigma_{\delta=0}^2(x_1) + \sigma^2(\delta)K^2\varepsilon_0\left[\left(\frac{1}{2}L_Q+L_\mathrm{d}\right)^2\beta_0\right. \\ & \left.+\frac{1}{4}L_Q^2L_\mathrm{d}^2\gamma_0 - L_Q^2L_\mathrm{d}^2\alpha_0\right]\end{aligned} \tag{20}$$

$$\begin{aligned}a = {} & \varepsilon_0\left[\left(\frac{1}{2}L_Q+L_\mathrm{d}\right)^2\beta_0 - \left(\frac{1}{2}L_Q^2L_\mathrm{d}+L_QL_\mathrm{d}^2\right)\alpha_0 + \frac{1}{4}L_Q^2L_\mathrm{d}^2\gamma_0\right] \\ & + \varepsilon_0\sigma^2(\delta)\left[\left(\frac{1}{2}L_Q+L_\mathrm{d}\right)^2\beta_0 + \frac{1}{4}L_Q^2L_\mathrm{d}^2\gamma_0 - L_Q^2L_\mathrm{d}^2\alpha_0\right]\end{aligned} \tag{21}$$

4.2 Verification via multiparticle simulations

Similar to the procedure discussed in Sect. 3.2, the system parameters of the HUST injector were fed into the ASTRA software for the beam dynamics calculations. By employing virtual measurements to assess the second-order correction effects, curves depicting the fluctuation of the measurement errors according to K_{range} under different energy-spread conditions were obtained, as shown in Fig. 5.

Figure 5a shows the measurement errors with second-order correction, excluding the chromatic effect. These errors are associated with the emittance derived by solving the coefficient equations Eq. (17) and post-parabolic fitting using Eq. (16). Compared with the measurement results shown in Fig. 4a, which do not undergo second-order correction, it is discernible that the measurement errors are generally reduced after second-order correction, even across various $\sigma(\delta)$ settings.

Furthermore, Fig. 5b shows the measurement errors after chromatic effect correction, aligned with the emittance determined via fitting using Eq. (20). Notably, building upon the second-order correction foundation, there is a further reduction in the measurement errors, especially when the energy spread is significant. Moreover, after all corrections outlined in this context, the relative beam emittance errors within the 0.1–6% energy spread range were reduced to approximately 1%. These results mark a significant advancement compared with the initial relative errors shown in Fig. 4a and b.

Additionally, to further highlight the versatility of the proposed correction methodology, additional beam dynamics simulations and virtual measurements were carried out for various beam emittances while maintaining a specific $\sigma(\delta)$ (0.27%), which was also obtained from the simulated beam parameters of the HUST injector, as listed in Table 1. The resulting measurement errors are shown in Fig. 6. Notably, compared with the emittance determined by the fitting coefficients of Eq. (13), the measurement approach with second-order correction corresponding to Eq. (20) demonstrates a relative-error-reduction capability of more than two-thirds within the normalized emittance range of 2–25 mm mrad. For clarity, Fig. 7 shows curves illustrating the measurement error fluctuations under a fixed K_{range} regarding the energy spread and emittance for various correction methods.

As shown in Fig. 7a, without chromatic effect correction (depicted by the dashed red and black lines corresponding to Eqs. (8) and (16), respectively), the emittance measurement errors exhibit a monotonically increasing trend as

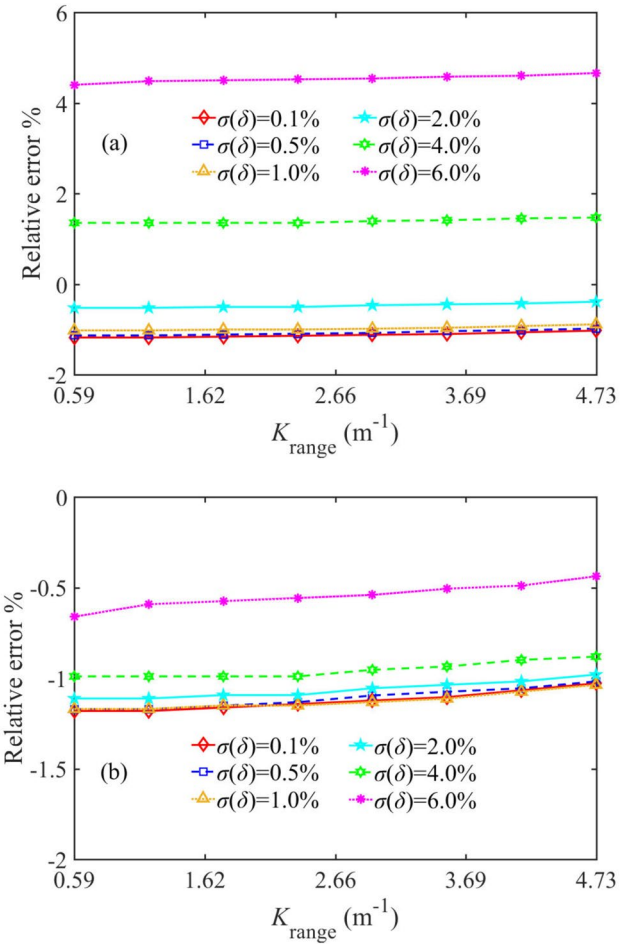

Fig. 5 Measurement errors under second-order correction with different $\sigma(\delta)$ settings: **a** without chromatic effect correction (Eq. 16), **b** with chromatic effect correction (Eq. 20)

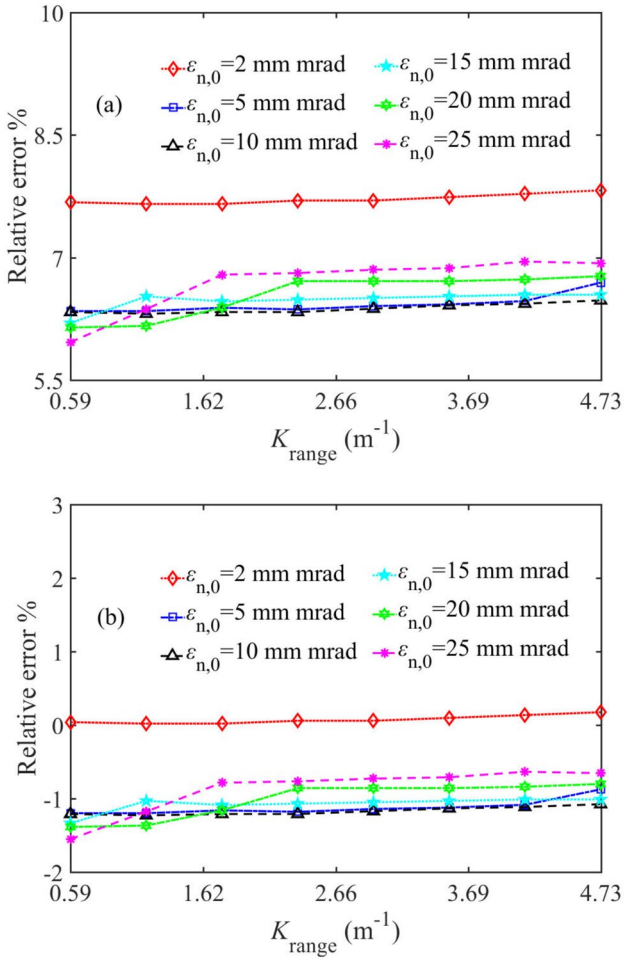

Fig. 6 Measurement errors under chromatic effect correction with different emittance settings: **a** traditional method (Eq. 13), **b** with second-order (Eq. 20), where $\varepsilon_{n,0}$ denotes the normalized emittance

$\sigma(\delta)$ increases. The traditional Q-scanning method exhibited improved error consistency after chromatic effect correction (depicted by the dotted blue line corresponding to Eq. (13)); however, the measurement error remained at approximately 7% for different $\sigma(\delta)$. Nonetheless, after second-order correction and considering chromatic effect elimination (depicted by the dotted green line corresponding to Eq. (20)), the absolute relative error decreased to less than 1.15%. Similarly, Fig. 7b shows a comparison between the measurement errors for different correction methods across various emittances. It is evident that the measurement errors are reduced by more than two-thirds after second-order correction, aligning with the discussion of the results shown in Fig. 6.

4.3 Validation for the HUST injector

The schematic of the HUST injector is shown in Fig. 8a. Transverse sizes can be measured on Fluorscreens using 16-bit digital cameras. Two fast current transformers (FCTs) were employed to separately measure the macroscopic beam current and length. An energy analysis system, consisting of a magnetic spectrometer (AM) and two Fluorscreens settled upstream (Flag) and downstream (Screen1), was used to measure the beam energy and energy spread.

Note that although there are three Q-magnets originally used for beam transport in the beam line, to reduce interference items in the emittance measurement, only Q1 associated with Screen2 was selected, while the other two Q-magnets were not in the working state. Because all simulations were performed using the beam parameters and system configurations of the HUST injector, it is reasonable to extend the application of the proposed methods to the experimental results obtained from the HUST injector. The corresponding beam spot size data and fitted curves are shown in Fig. 8b. The measurement results are presented in Table 2.

It is worth noting that the dotted red line in Fig. 8b represents the original fitting curve, and the corresponding emittance measurement value determined based on it is listed in

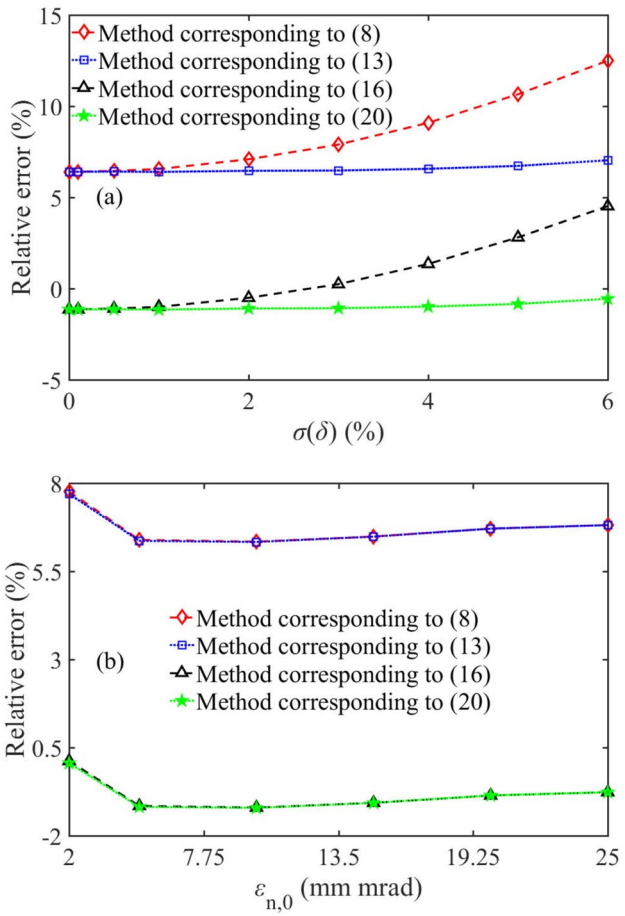

Fig. 7 Measurement error variations under different correction methods: **a** along with $\sigma(\delta)$ at a specific emittance of $\varepsilon_{n,0}$ = 4.9 mm mrad, **b** along with $\varepsilon_{n,0}$ at $\sigma(\delta)$ = 0.27%

Table 2 as "original result," from which the energy spread influence is already excluded, as reported in [35]. Furthermore, leveraging the use of fixed vertices, as discussed in Sect. 3, the result is reduced to 8.6 mm mrad. Although this improvement appears modest, the comprehensive application of the proposed correction methods, corresponding to Eq. (20), yields the corrected result of 7.9 mm mrad, which is determined from the fitting curve depicted by the dashed blue line in Fig. 8b. This value is close to the simulation value of 4.9 mm mrad, as listed in Table 1. The main contribution of this study is the emittance measurement accuracy and result consistency improvement by improving both the pre- and post-processing methods for the experimental data. Such an enhanced approach could be used as a general processing method for measuring emittance based on *Q*-scanning techniques. The remaining discrepancy might be attributed to the effects of the space charge and long-range wake fields, which have already been discussed previously [35] and are beyond the scope of the current study. Further investigations will be undertaken to analyze the measurement effects induced by factors such as the beam spot size and regularity.

5 Conclusion

Precise emittance measurements are of paramount importance for the design, commissioning, and application of beam injectors. Measurement methods based on *Q*-scanning techniques are widely used for injectors. However, in previous studies, several implicit assumptions were made for simplification, and ignored factors may produce inevitable measurement errors in real-world applications.

To enhance *Q*-scanning-based diagnostic methods for evaluating the transverse emittance in beam injectors, a thorough review of the fundamental principles underlying the *Q*-scanning method was performed. Subsequently, a theoretical analysis was conducted to assess the impact of various factors on data processing, including the range of independent variable values and fitting parabolic vertex position. The contribution of the energy spread to the emittance measurement errors was also examined through both analytical derivations and multiparticle simulations. Furthermore, based on the analysis results, a new fitting formula was derived incorporating second-order terms of the transfer matrix elements and considering the influence of the energy spread within the *Q*-scanning technique. Using a HUST injector as a case study, comprehensive beam dynamics calculations were performed to verify the analytical results through virtual measurements. Additionally, actual emittance measurements at the HUST injector were corrected using the proposed methodology, resulting in outcomes that closely aligned with the physical design expectations, thereby validating the reliability of the proposed compensation to a considerable extent.

In summary, the collective efforts undertaken in this study showcase the enhanced abilities of the *Q*-scanning method, providing effective corrections for the experimental emittance measurement results. These advancements have the potential to foster the development of *Q*-scanning techniques, including their applications in various beam injectors.

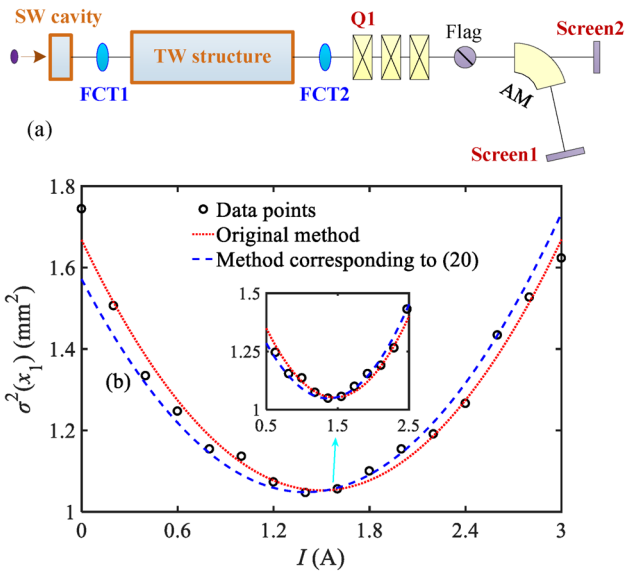

Fig. 8 **a** Schematic of the HUST injector; **b** Experimental emittance measurement data for the HUST injector

Table 2 Emittance measurements conducted at the HUST injector

Method	Experimental results
Original method	8.8 mm mrad
Correction corresponding to (8)	8.6 mm mrad
Correction corresponding to (20)	7.9 mm mrad

Author contributions All authors contributed to the study conception and design. Material preparation, data collection, and analysis were performed by Yi-Feng Zeng, Tong-Ning Hu, and Hao Hu. The first draft of the manuscript was written by Yi-Feng Zeng and Tong-Ning Hu, and all authors commented on previous versions of the manuscript. All authors read and approved the final manuscript.

Data availability statement The data that support the findings of this study are openly available in Science Data Bank at https://cstr.cn/31253.11.sciencedb.j00186.00313 and https://www.doi.org/10.57760/sciencedb.j00186.00313.

Declarations

Conflict of interest The authors declare that they have no conflict of interest.

References

1. S.G. Biedron, J.W. Lewellen, S.V. Milton et al., Compact, high-power electron beam based terahertz sources. Proc. IEEE **95**(8), 1666–1678 (2007). https://doi.org/10.1109/JPROC.2007.898858
2. R. Wang, C. Qian, Y.H. Guo et al., Automatic spectrum recognition system for charge state analysis. Aip Conf. Proc. Nucl. Sci. Tech. **34**, 178 (2023). https://doi.org/10.1007/s41365-023-01326-9
3. N.S. Huang, Z.P. Liu, B.J. Deng et al., The MING proposal at SHINE: megahertz cavity enhanced X-ray generation. Nucl. Sci. Tech. **34**, 6 (2023). https://doi.org/10.1007/s41365-022-01151-6
4. D.H. Jeong, M. Lee, H. Lim et al., Electron beam scattering device for FLASH preclinical studies with 6-MeV LINAC. Nucl. Eng. Technol. **53**, 1289–1296 (2021). https://doi.org/10.1016/j.net.2020.09.019
5. J.X. Wang, K. Zhou, P. Li et al., High-brightness photo-injector with standing-wave buncher-based ballistic bunching scheme for inverse Springer Tr Mod Phys light source. Nucl. Sci. Tech. **33**, 44 (2022). https://doi.org/10.1007/s41365-022-01025-x
6. T.N. Hu, Y.J. Pei, G.Y. Feng, Electron beamline of a Linac-based injector applied to a compact free electron laser-terahertz radiation source. Jpn. J. Appl. Phys. **57**, 100310 (2018). https://doi.org/10.7567/JJAP.57.100310
7. K. Flöttmann, RF-induced beam dynamics in rf guns and accelerating cavities. Phys. Rev. Spec. Top-Ac **18**, 064801 (2015). https://doi.org/10.1103/PhysRevSTAB.18.064801
8. H. Chen, L.M. Zheng, B. Gao et al., Beam dynamics optimization of very-high-frequency gun photoinjector. Nucl. Sci. Tech. **33**, 116 (2022). https://doi.org/10.1007/s41365-022-01105-y
9. H.M. Xie, K.W. Gu, Y. Wei et al., A noninvasive ionization profile monitor for transverse beam cooling and orbit oscillation study in HIRFL-CSR. Nucl. Sci. Tech. **31**, 40 (2020). https://doi.org/10.1007/s41365-020-0743-7
10. X.C. Lin, H. Zha, J.R. Shi et al., Development of a seven-cell S-band standing-wave RF-deflecting cavity for Tsinghua Thomson scattering X-ray source. Nucl. Sci. Tech. **32**, 36 (2021). https://doi.org/10.1007/s41365-021-00871-5
11. T.N. Hu, J.Y. Li, Y.J. Pei et al., Indirect estimations of energy and energy spread for a compact free electron laser-terahertz pre-injector using RF measuring parameters. Nucl. Instrum. Methods A **1016**, 165775 (2021). https://doi.org/10.1016/j.nima.2021.165775
12. T.N. Hu, B.Q. Zeng, G.Y. Feng et al., Compensation and improvement for bunch length diagnostics based on RF-phasing techniques. Nucl. Instrum. Methods A **1011**, 165583 (2021). https://doi.org/10.1016/j.nima.2021.165583
13. Y. Bian, W.Y. Zhang, B. Liu et al., Sub-picosecond electron bunch length measurement using coherent transition radiation at SXFEL. Nucl. Sci. Tech. **29**, 74 (2018). https://doi.org/10.1007/s41365-018-0399-8
14. Z.Y. Dai, Y.C. Nie, Z. Hui et al., Design of S-band photoinjector with high bunch charge and low emittance based on multi-objective genetic algorithm. Nucl. Sci. Tech. **34**, 41 (2023). https://doi.org/10.1007/s41365-023-01183-6
15. S. Weathersby, G. Brown, M. Centurion et al., Mega-electron-volt ultrafast electron diffraction at SLAC national accelerator laboratory. Rev. Sci. Instrum. **86**, 073702 (2015). https://doi.org/10.1063/1.4926994
16. L. Zheng, Y. Du, P. Huang, Eliminating uncertainty of thermal emittance measurement in solenoid scans due to rf and solenoid fields overlap. Nucl. Instrum. Methods A **1025**, 166149 (2022). https://doi.org/10.1016/j.nima.2021.166149
17. A. Wolski, D.C. Christie, B.L. Militsyn et al., Transverse phase space characterization in an accelerator test facility. Phys. Rev. Accel. Beams **23**, 032804 (2020). https://doi.org/10.1103/PhysRevAccelBeams.23.032804
18. M.J. Wu, D.Y. Li, J.G. Zhu et al., Emittance measurement along transport beam line for laser driven protons. Phys. Rev. Accel. Beams **23**, 031302 (2020). https://doi.org/10.1103/PhysRevAccelBeams.23.031302
19. K. Jiang, K. Feng, H. Wang et al., Measurement of electron beam transverse slice emittance using a focused beamline. High Power Laser Sci. Eng. **11**, e36 (2023). https://doi.org/10.1017/hpl.2023.9
20. H. Chen, L. Zheng, P. Huang et al., Analysis of slice transverse emittance evolution in a very-high-frequency gun photoinjector. Phys. Rev. Accel. Beams **24**, 124402 (2021). https://doi.org/10.1103/PhysRevAccelBeams.24.124402
21. J.H. Lee, J.H. Han, J. Hong et al., Slice emittance measurement using rf deflecting cavity at PAL-XFEL ITF, in Proceedings of the Free-Electron Laser Conference, pp 707–709 (2014)
22. L. Feigin, A. Weinberg, A. Nause, Algorithm verification of single-shot relativistic emittance proposed measuring method. Electronics **11**, 2092 (2022). https://doi.org/10.3390/electronics11132092
23. S. Ma, A. Arnold, P. Michel et al., The application of encoder–decoder Neural Networks in high accuracy and efficiency slit-scan emittance measurements. Nucl. Instrum. Methods A **1050**, 168125 (2023). https://doi.org/10.1016/j.nima.2023.168125
24. Y.C. Feng, M. Li, R.S. Mao et al., Transverse emittance measurement for the heavy ion medical machine cyclotron. Nucl. Sci. Tech. **30**, 184 (2019). https://doi.org/10.1007/s41365-019-0699-7
25. W.X. Wang, C. Li, Z.G. He et al., Commissioning the photocathode radio frequency gun: a candidate electron source for Hefei Advanced Light Facility. Nucl. Sci. Tech. **33**, 23 (2022). https://doi.org/10.1007/s41365-022-01000-6
26. P. Forck, Lecture notes on beam instrumentation and diagnostics. Joint Universities Accelerator School (JUAS 2010) (2011)
27. S.H. Wang, Q. Ye, J.S. Cao et al., Emittance measurement by multi-changing focusing strength. Chin. Phys. C **26**, 1184–1188 (2002)
28. F. Löhl, S. Schreiber, M. Castellano et al., Measurements of the transverse emittance at the FLASH injector at DESY. Phys. Rev. Spec. Top-Ac **9**, 092802 (2006). https://doi.org/10.1103/PhysRevSTAB.9.092802
29. E. Prat, M. Aiba, Four-dimensional transverse beam matrix measurement using the multiple-quadrupole scan technique. Phys. Rev. Spec. Top-Ac **17**, 052801 (2014). https://doi.org/10.1103/PhysRevSTAB.17.052801
30. S.G. Anderson, J.B. Rosenzweig, G.P. LeSage et al., Space-charge effects in high brightness electron beam emittance measurements. Phys. Rev. Spec. Top-Ac **5**, 014201 (2002). https://doi.org/10.1103/PhysRevSTAB.5.014201
31. A. Mostacci, M. Bellaveglia, E. Chiadroni et al., Chromatic effects in quadrupole scan emittance measurements. Phys. Rev. Spec. Top-Ac **15**, 082802 (2012). https://doi.org/10.1103/PhysRevSTAB.15.082802
32. M. Olvegård, V. Ziemann, Effect of large momentum spread on emittance measurements. Nucl. Instrum. Methods A **707**, 114–119 (2013). https://doi.org/10.1016/j.nima.2012.12.114
33. K. Poorrezaei, R.B. Fiorito, R.A. Kishek et al., New technique to measure emittance for beams with space charge. Phys. Rev. Spec. Top-Ac **16**, 082801 (2013). https://doi.org/10.1103/PhysRevSTAB.16.082801
34. B.E. Carlsten, Characterizing the emittance contribution due to rotated quadrupoles and canonical angular momentum using the quadrupole scan technique in electron accelerators. Rev. Sci. Instrum. **70**, 1672–1683 (1999). https://doi.org/10.1063/1.1149650

35. T.N. Hu, Y.J. Pei, B. Qin et al., Development of a novel thermionic RF electron gun applied on a compact THz-FEL facility. Nucl. Instrum. Methods A **887**, 1–6 (2018). https://doi.org/10.1016/j.nima.2017.12.070
36. K. Flöttmann, ASTRA: a space charge tracking algorithm, user manual (2017)